Nanoscale

Spin defects in hexagonal boron nitride for strain sensing on nanopillar arrays

Journal:	*Nanoscale*
Manuscript ID	NR-ART-12-2021-007919.R3
Article Type:	Paper
Date Submitted by the Author:	14-Mar-2022
Complete List of Authors:	Yang, Tieshan; University of Technology Sydney, School of Mathematical and Physical Sciences Mendelson, Noah; University of Technology Sydney, School of Mathematical and Physical Sciences Li, Chi; University of Technology, Sydney, Gottscholl, Andreas ; Julius Maximilian University of Würzburg, Experimental Physics 6 and Würzburg-Dresden Cluster of Excellence Scott, John; University of Technology Sydney Kianinia, Mehran; University of Technology Sydney, School of Mathematical and Physical Sciences Dyakonov, Vladimir; Julius Maximilian University of Würzburg, Experimental Physics 6 and Würzburg-Dresden Cluster of Excellence Toth, Milos; University of Technology, Sydney, School of Physics and Advanced Materials Aharonovich, Igor; University of Technology, Sydney,

Nanoscale

Spin defects in hexagonal boron nitride for strain sensing on nanopillar arrays

Received 00th December 2021,
Accepted 00th December 2021

DOI: 10.1039/x0xx00000x

Tieshan Yang,[‡a,b] Noah Mendelson,[‡a] Chi Li,[a] Andreas Gottscholl,[c] John Scott,[a,b] Mehran Kianinia,*[a] Vladimir Dyakonov,[c] Milos Toth,[a,b] Igor Aharonovich*[a,b]

Two-dimensional hexagonal boron nitride (hBN) has attracted much attention as a platform for studies of light-matter interactions at the nanoscale, especially in quantum nanophotonics. Recent efforts have focused on spin defects, specifically negatively charged boron vacancy (V_B^-) centers. Here, we demonstrate a scalable method to enhance the V_B^- emission using an array of SiO_2 nanopillars. We achieve a 4-fold increase in photoluminescence (PL) intensity, and a corresponding 4-fold enhancement in optically detected magnetic resonance (ODMR) contrast. Furthermore, the V_B^- ensembles provide useful information about the strain fields associated with the strained hBN at the nanopillar sites. Our results provide an accessible way to increase the emission intensity as well as the ODMR contrast of the V_B^- defects, while simultaneously form a basis for miniaturized quantum sensors in layered heterostructures.

Introduction

Optically active spin defects in three-dimensional wide band-gap semiconductors have shown great potential in both fundamental and practical applications in quantum information processing and high−resolution quantum sensing.[1-6] The accelerating progress in studies and engineering of novel two dimensional (2D) systems and van der Waals heterostructures has sparked an interest to investigated spin systems in these materials.[7-9] To this extent, hexagonal boron nitride (hBN) has gained increased attention as an alternative candidate for studying spin based phenomena in van der Waals crystals due to its large bandgap and optical transparency.[10] In addition, hBN hosts a large variety of optically active defects,[11-15] some of which have recently been shown to have access to its spin state.[16-18]

A particular spin defect that garners significant attention is the negatively charged boron vacancy (V_B^-).[19-31] The (V_B^-) spin can be initialized, manipulated, and read out optically, with coherence times on the order of several microseconds at room temperature.[17] The V_B^- defect has a triplet ground state with a zero-field splitting (ZFS) D_{gs}/h of ~3.46 GHz and a broad emission around 800 nm. The spin orientation of V_B^- is known to be out of plane. The defect can be generated by neutron irradiation, ion implantation, laser ablation, and electron irradiation, and they have been shown to be a promising candidate for temperature, pressure, and magnetic field sensing in van der Waals materials.

On the other hand, the relatively low brightness of the V_B^- defects is a major issue in acquiring the optically detected magnetic resonance (ODMR) contrast. To overcome this problem a few approaches based on coupling to dielectric of plasmonic cavities have been attempted. For instance, through coupling of V_B^- defects to dielectric bullseye,[32] plasmonic cavities,[33] the photoluminescence (PL) of V_B^- emitters has been dramatically enhanced. Future integration of spin defects in photonic cavities or waveguides is ultimately required to improve photon collection efficiencies and realize nanoscale quantum sensing and integrated quantum circuitry.

In this work, we integrate the V_B^- spin defects embedded in a few layer hBN with dielectric nanopiallar arrays. We investigate the enhancement in photoluminescence from the V_B^- defects and the associated ODMR contrast. We observed a PL intensity enhancement of ~4-times by the nanopillars and a corresponding improvement in measured ODMR contrast. Furthermore, we show the applicability of V_B^- defects as a nano strain sensor for measuring the local strain in hBN across the nanopillars.

Results and discussion

Nanopillar arrays were fabricated from a Si substrate with a 285 nm thermal silicon oxide layer. The nanopillar diameter and spacing are defined by electron beam lithography (EBL) using a polymethyl methacrylate (PMMA) positive resist and nickel as a hard mask for reactive ion etching (see the Methods section). The fabricated nanopillar arrays were thoroughly cleaned and high quality exfoliated hBN flakes were transferred onto the nanopillars. Figure 1a shows a schematic illustration of a nanopillar and a hBN film containing the V_B^- defect. The pillars used in this work have a height *h* of 350 nm, diameter *d* of 500 nm, and a spacing *s* of 6 µm. The pillar quality was evaluated by scanning electron microscopy (SEM) as is shown in Figure 1b. Figure 1c shows an optical image of

[a] School of Mathematical and Physical Sciences, Faculty of Science, University of Technology Sydney, Ultimo, New South Wales 2007, Australia
Email: mehran.kianinia@uts.edu.au; igor.aharonovich@uts.edu.au
[b] ARC Centre of Excellence for Transformative Meta-Optical Systems (TMOS), University of Technology Sydney, Ultimo, New South Wales 2007, Australia
[c] Experimental Physics 6 and Würzburg-Dresden Cluster of Excellence, Julius Maximilian University of Würzburg, Würzburg, Germany
‡These authors contributed equally

the array after hBN film transfer. The thickness of the hBN flake was determined to be ~17 nm by Atomic Force Microscope. The hBN flakes were cleaned using a UV ozone generator for 10 min to remove tape residuals before ion irradiation. Boron vacancies (V_B^-) were generated by focused nitrogen ion beam (FIB) irradiation at normal incidence in a plasma-source FIB system (Thermo Scientific Helios G4 Hydra). The top region was irradiated with an ion beam fluence of 1 × 10^{14} ions cm^{-2}, whilst the fluence for the bottom region was 1 × 10^{12} ions cm^{-2}. The ion energy and current 30 keV and 1.9 pA, respectively.

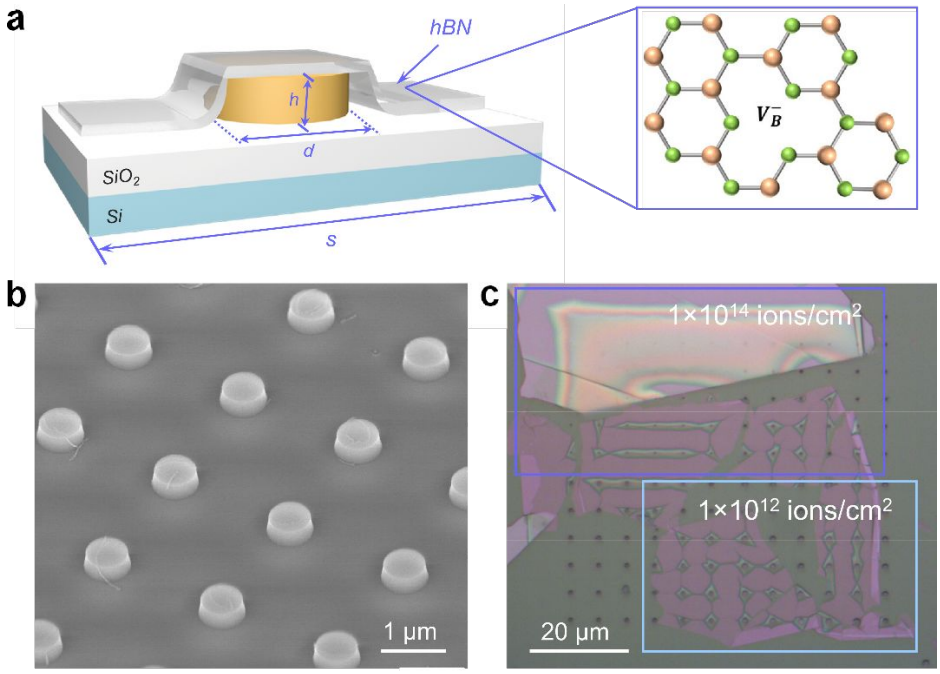

Figure 1. (a) Schematic illustration of a nanopillar with a hBN overlayer. The nanopillars have a height h of 350 nm, diameter d of 500 nm, and spacing s of 6 µm. The insert is an illustration of the boron vacancy (V_B^-) defect in hBN, with boron and nitrogen atoms shown as green and orange spheres, respectively. (b) Scanning electron microscope image of a nanopillar array. (c) Optical image of array with a transferred hBN overlayer. The top region was irradiated with an ion beam fluence of 1 × 10^{14} ions cm^{-2}, whilst the fluence for the bottom region was 1 × 10^{12} ions cm^{-2}.

Comprehensive measurements were performed to compare the PL emission from V_B^- ensembles on and off the SiO_2 nanopillars using a home-built scanning confocal optical microscope. Figure 2a shows a PL intensity map of the sample, in which red spots suggest emission enhancement caused by nanopillars. White circles highlight two spots where V_B^- defects are on the top of nanopillars (marked as pillar 1 and 2). Figures 2b, c show PL spectra from the pillars (red), and corresponding spectra from uncoupled V_B^- emissions (blue) taken from regions of the hBN flake adjacent to the pillars using a 532 nm continuous wave excitation laser with a power of 3 mW. The spectra clearly show that the V_B^- emission is enhanced at both pillar sites. On pillar 1, the peak height is ~4 times greater than that of the reference spectrum, indicating significant enhancement of the V_B^- emission by the pillar. Similarly, on pillar 2, the V_B^- emission intensity is ~2.5 times greater than in the reference spectrum. Note that in the calculation of peak height, we assumed a linear background emission which is subtracted from each spectrum. Enhancement in this range was observed for all pillar sites across the sample. Since ion implantation was done normal to the substrate, vacancy generation would be higher on the side of the pillar where the incident angle is smaller. On the contrary the PL scans indicate higher PL emission from top of the pillars. Nanoscale dielectric pillars have been used to PL emission from embedded color centres in diamond and silicon carbide, as well as emission from 2D materials.[34-36] This effect is predominantly due to an enhanced light collection since the pillars act as an antenna. We note that no lifetime modification and no Purcell enhancement is observed in this case.

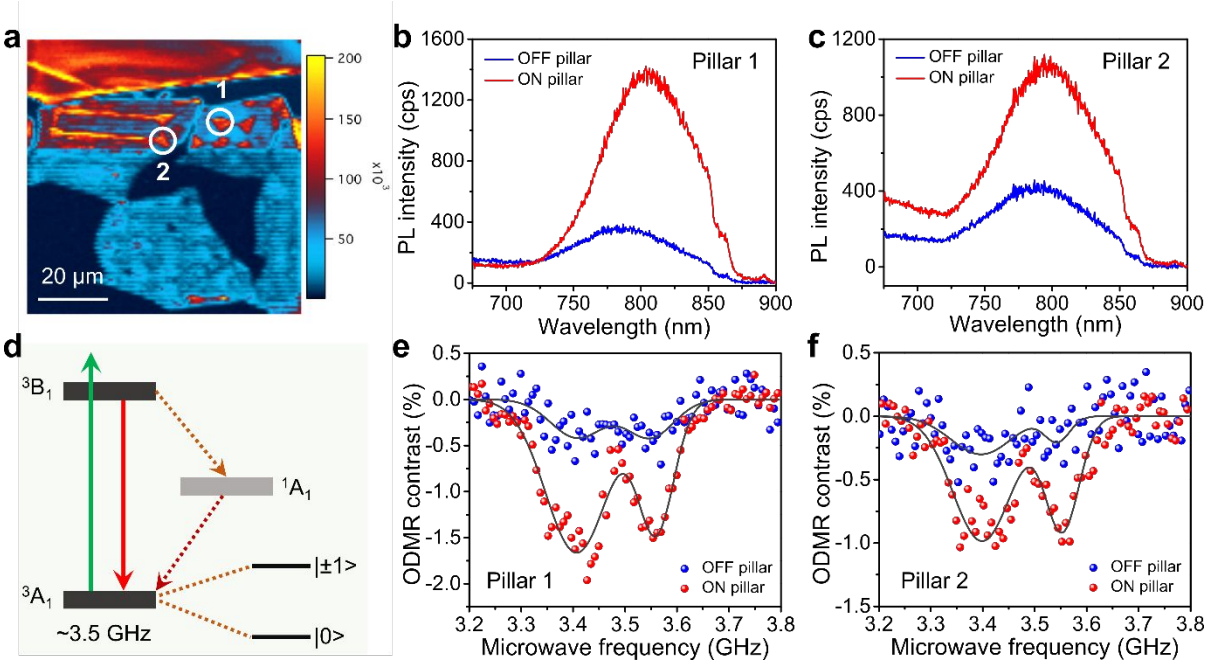

Figure 2. (a) Confocal PL intensity map generated by integrating spectra between 715 and 900 nm. White circles highlight spots corresponding to two nanopillars labelled 1 and 2. (b, c) PL spectra of V_B^- ensembles located on (red) and off (blue) the nanopillars. The sample was excited with a 532nm continuous wave laser with a power of 3 mW. The integration time was 10 s. (d) Level structure of the V_B^- spin defect with a triplet ground state, indicated by 0 and ±1 states. (e, f) ODMR spectra of the V_B^- ensembles located on (red) and off (blue) nanopillars 1 and 2, and two-Lorentzian fits of the spectra (black).

To showcase the spin readout capability of the V_B^- ensembles, we performed ODMR spectroscopy at room temperature. A schematic illustration of the level structure of a V_B^- spin defect is shown in Figure 2d and ODMR spectra taken on and off nanopillars 1 and 2 are shown in Figure 2e and f, respectively. The V_B^- spin defect has a triplet ground state with a ground state splitting of ~3.5 GHz between the m_s = 0 and m_s = ±1 states. For the ODMR measurements, a thin copper wire (with a diameter of ~ 20 μm) was suspended in a close proximity (~10 μm) to the region of interest and used as an antenna to deliver a microwave field. The PL emission (spectral range 720–900 nm) was recorded as the microwave frequency was swept from 3.2 to 3.8 GHz. The fluorescence signal decreases at microwave frequencies ν_1 of ~ 3.41 GHz and ν_2 of ~ 3.51 GHz. The ODMR spectra were fitted with two Lorentzian functions. The V_B^- defect has a triplet (S = 1) ground state with a zero-field splitting defined by the parameters D_{gs} and E_{gs}. We find that $D_{gs} \cong 3.46$ GHz and $E_{gs} \cong 50$ MHz. The triplet energy sublevels have a completely lifted threefold degeneracy even in the absence of an external magnetic field. The resonant frequencies ν_1 and ν_2 in the ODMR spectra are given by $\nu_{1,2} = D_{gs}/h \pm (1/h)\sqrt{E_{gs}^2 + (g\mu_B B)^2}$ where g is the Landé factor and μ_B is the Bohr magneton. Our measurements were performed in the absence of external magnetic fields, thus $\nu_{1,2} = (D_{gs} \pm E_{gs})/h$.

The ODMR spectra in Figures 2e and f demonstrate significant enhancement of ODMR contrast at the nanopillar sites. Specifically, because of an improved PL signal-to-background ratio, the ODMR signal from V_B^- on nanopillar 1 has an optical contrast of ~1.7%, which is four times greater than that of the reference signal from a pristine V_B^- ensemble (~0.4%). Similarly, on pillar 2, the ODMR contrast is ~1%, as compared to ~0.3% for the pristine V_B^- ensemble. In this case the hBN flake has not completely covered the pillar compared to the one on top of pillar one wrestling in less enhancement of PL emission and ODMR contrast.

Overall, the ODMR contrast from spin defects in hBN is still under debate.[18, 24, 37] An improved signal to background ratio can result in a better contrast. In addition, the strain can affect the overall transition rates within the V_B^- level manifold and change the rates to/from the metastable state, hence increasing the ODMR contrast. Changes to ODMR contrast have been also reported for both diamond and silicon carbide, whereby induction of non-radiative recombination (either via surrounding defects or temperature) resulted in a reduced contrast.[38, 39] Furthermore, for some spin defects in hBN, the ODMR contrast can be both positive or negative, and its

magnitude can vary,[18] most likely, due to the modification of the transition rates from the various sub levels. While this will trigger further research, the improved ODMR contrast and enhanced PL signal-to-noise ratio are important outcomes that can yield significant improvements in readout and help enable integration of practical hBN sensors in 2D heterostructures for quantum sensing applications.

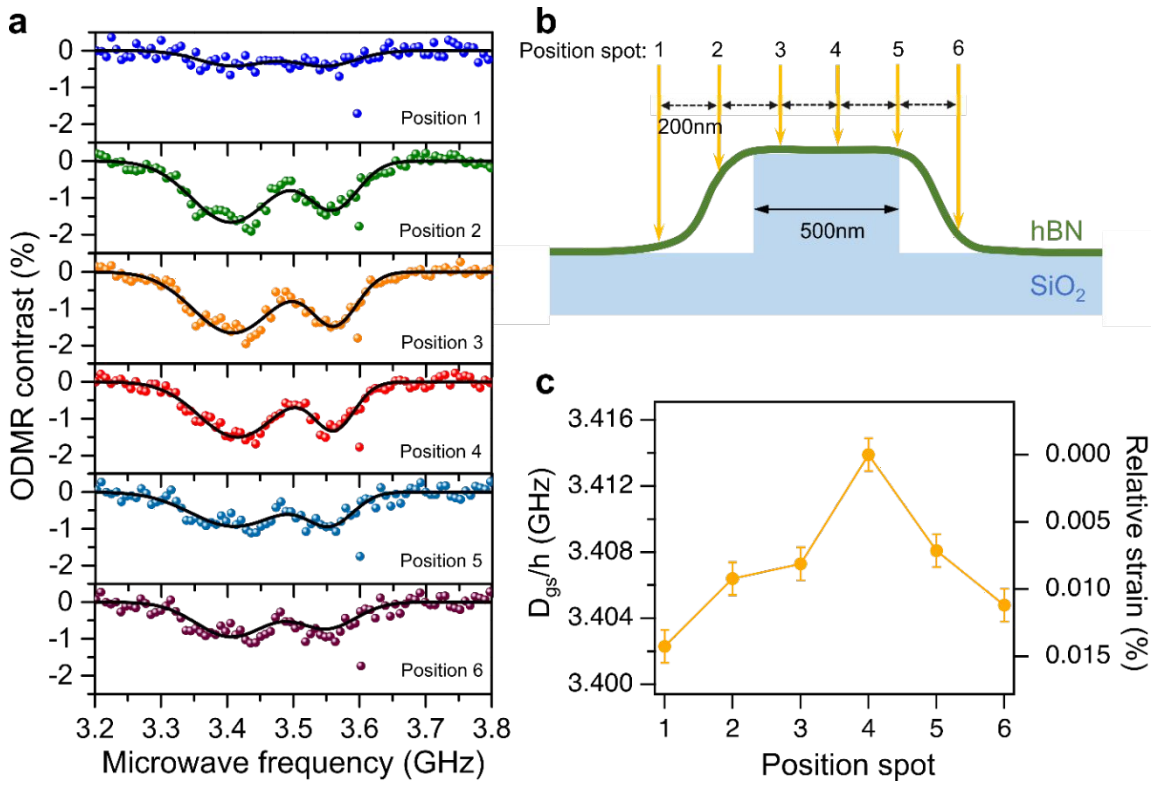

Figure 3. Dependence of V_B^- ODMR spectra on position across a single nanopillar. (a) ODMR spectra at different positions and the theoretical two-Lorentzian fits. The upper two pictures and the lower one figures were measured off a nanopillar, and the middle three were measured on the pillar. (b) Schematic drawing of a cross section of hBN laying on top of a nanopillar. The yellow arrows represent the spot positions where the ODMR measurements were performed. (c) The ZFS parameter and the strain as a function of different positions. A reduced ZFS parameter corresponds to an in-plane strain (see right y-axis).

To gain more insight into the strain effect on the V_B^- defect at different nanopillar positions, we performed ODMR measurements across one nanopillar. The distance between each different position is about ~200 nm, which is determined using the piezo stage.

Position-dependence of ODMR signals for V_B^- defects are shown in Figure 3. As we can see in Figure 3a, there is a clear trend of the ODMR contrast at different nanopillar positions. In the region of nanopillars (see Figure 3b for illustration), the ODMR has a contrast of about ~1.7%, while off nanopillars, the ODMR contrast is about ~ 0.4-1%, indicating there is a stain effect on the nanopillar. Although ODMR contrast is very low outside the pillar, it can be improved by using resonators such as plasmonic structure. Nevertheless, to support this assumption, we analyzed the observed ZFS parameters quantitatively. As previously discussed, the ODMR signal can be fitted by two Lorentzian functions with the resonance frequencies $\nu_{1,2} = (D_{gs} \pm E_{gs})/h$. However, in general the ZFS parameter is not constant since it is affected by the sample temperature and local lattice strains around the V_B^- defect. Assuming a constant temperature during the measurements we can describe the observed ZFS parameter D_{gs} with

$$D_{gs} = D_{gs,0} + \Delta D_{gs,a} + \Delta D_{gs,c}$$

The ZFS parameter consists of a reference value $D_{gs,0}$ which is shifted by $\Delta D_{gs,a}$ and $\Delta D_{gs,c}$ according to an in-plane lattice strain η_a and an inter-plane lattice strain η_c, respectively. Due to the covering of the nanopillars, the hBN flake is mainly stretched in the plane and a compression in c-direction is not to be expected. Therefore, the influence of strains can be reduced to $\Delta D_{gs,a} = \theta_a \eta_a h$ with the proportionality factor $\theta_a = (-81 \pm 12)\, GHz$. The strain field created by putting a 2D materials on top of pillars is well understood and has been reported in many works using Raman or SHG.[36, 40-42] In Figure 3c we extracted the different ZFS parameters D_{gs} for each spot position. To determine the corresponding relative strain η_a we choose arbitrary the spot position 4 for reference $D_{gs,0}$ since we expect the lowest influence of strain in the centre of a nanopillar. According to the ZFS shift we can extract a relative strain in the order of 0.01% (see right y-axis in

Figure 3c) across the nanopillar. This fits to the assumption that the hBN flake is stretched around the nanopillar.

Conclusions

In conclusion, we have demonstrated the integration of the defects in hBN on dielectric SiO_2 nanopillars. PL and ODMR of hBN V_B^- spin defects on nanopillars and off nanopillars are studied. hBN spin defects exhibit a ~4-fold enhancement in PL emission, associated with an improved ODMR contrast on the nanopillars (~1.7%) compared with pristine substrate (~0.4%). Furthermore, the ODMR contrast has a significant position-dependent on different pillar positions, indicating the strain effect from the pillar. This can be potentially useful to study strain effects in other 2D materials, *e.g.* transition metal dichalcogenides (TMDCs) that are placed on pillars to induce localized quantum emitters.[42, 43] Overall, our work strongly supports the promising potential of V_B^- defects as a nanoscale strain sensor in a 2D material platform.

Experimental methods

Nanopillar arrays fabrication

A pre-cleaned Si substrate (with a 285 nm thick thermally grown silicon dioxide layer) was spin-coated with PMMA (positive resist) under 3000 rpm, resulting in a ~200 nm thick resist film. Then, the substrate was put on a hotplate (180 ℃) for 3 min to evaporate the excess solvent. After this, the substrate was loaded into SEM (ZEISS supra 55VP) chamber which contains the electron beam lithography system (Raith Elphy Plus). PMMA exposure was performed through an electron beam fluence of 300 μC/cm^2. The irradiated regions were removed using a 1:3 solution of methyl isobutyl ketone (MIBK) and isopropyl alcohol (IPA). Then, a thickness of 150 nm nickel was deposited in a vacuum sputtering chamber. The lift-off process was performed in hot acetone, leaving only nickel mask in the patterned areas. Inductively coupled plasma (ICP) reactive ion etching (RIE) was then used to etch the SiO_2 substrate. During the etching process, the chamber pressure was set to 4 mTorr, and plasma powers of 500 W and 70 W were used for the ICP and the radio frequency power. Gas flow rates were set to 10 sccm for Ar and 50 sccm for SF_6, respectively. The etching rate was ~ 5 nm/s. The top protective nickel masks were dissolved in dilute HCl solution (2M) overnight, yielding nanostructured pillars for subsequent high quality hBN transfer.

hBN transfer to pillar arrays

High quality exfoliated hBN flakes were accurately transferred onto the fabricated nanopillars using a polyvinyl alcohol (PVA) assisted align transfer method. The PVA layer was removed by immersion in hot water for 1 hour, then put into a vacuum chamber for an hour to dry.

Finally, the flakes were cleaned in a UV–ozone generator for 10 min to remove the tape residuals before irradiation.

hBN irradiation

Boron vacancies (V_B^-) were created by focused ion beam irradiation at normal incidence in a plasma focused ion beam (FIB) system using a nitrogen source (Thermo Scientific Helios G4 Hydra). The ion beam fluence, energy and current were 1×10^{14} ions cm^{-2} (1×10^{12} ions cm^{-2}) 30 keV and 1.9 pA, respectively.

Photoluminescence spectroscopy and ODMR measurement

A home-built scanning confocal microscopy system comprising a microwave system was used for the ODMR measurement. A 532 nm continuous wave laser was focused on the samples through an objective (NA = 0.9, 100 × magnification) for spin initialization and excitation. The reflection signal was spectrally filtered using a 532 nm dichroic mirror (LP03-532RE-25) and a 715 nm long pass filter to guide through a fiber to an avalanche photodiode (APD, Excelitas) for signal readout. In the microwave system, the microwave irradiation generated by a synthesized signal generator (AnaPico APSIN) went through a microwave switch and an amplifier (mini circuits, ZHL-16W-43-S+), and then a 20 μm diameter copper wire suspended in proximity (~10 μm away) to the samples served as an antenna to deliver the microwave field. The contrast was then calculated from the acquired signal in each frequency value.

Conflicts of interests

The authors declare no competing financial interest.

Acknowledgements

The authors acknowledge financial support from the Australian Research Council (CE200100010), the Asian Office of Aerospace Research & Development (FA2386-20-1-4014) and the Office of Naval Research Global (N62909-22-1-2028). The authors thank the Australian Nanofabrication Facilities at the UTS OptoFab node.

References

1. M. Atatüre, D. Englund, N. Vamivakas, S.-Y. Lee and J. Wrachtrup, Nature Reviews Materials, 2018, 3, 38-51.
2. D. D. Awschalom, R. Hanson, J. Wrachtrup and B. B. Zhou, Nature Photonics, 2018, 12, 516-527.
3. C. L. Degen, F. Reinhard and P. Cappellaro, Reviews of Modern Physics, 2017, 89, 035002.
4. W. B. Gao, A. Imamoglu, H. Bernien and R. Hanson, Nature Photonics, 2015, 9, 363-373.
5. C. E. Bradley, J. Randall, M. H. Abobeih, R. C. Berrevoets, M. J. Degen, M. A. Bakker, M. Markham, D. J. Twitchen and T. H. Taminiau, Physical Review X, 2019, 9, 031045.

6. C. Babin, R. Stöhr, N. Morioka, T. Linkewitz, T. Steidl, R. Wörnle, D. Liu, E. Hesselmeier, V. Vorobyov, A. Denisenko, M. Hentschel, C. Gobert, P. Berwian, G. V. Astakhov, W. Knolle, S. Majety, P. Saha, M. Radulaski, N. T. Son, J. Ul-Hassan, F. Kaiser and J. Wrachtrup, Nature Materials, 2022, 21, 67-73.
7. A. K. Geim and I. V. Grigorieva, Nature, 2013, 499, 419-425.
8. A. Rodin, M. Trushin, A. Carvalho and A. H. Castro Neto, Nature Reviews Physics, 2020, 2, 524-537.
9. X. Liu and M. C. Hersam, Nature Reviews Materials, 2019, 4, 669-684.
10. J. D. Caldwell, I. Aharonovich, G. Cassabois, J. H. Edgar, B. Gil and D. N. Basov, Nature Reviews Materials, 2019, 4, 552-567.
11. N. Mendelson, D. Chugh, J. R. Reimers, T. S. Cheng, A. Gottscholl, H. Long, C. J. Mellor, A. Zettl, V. Dyakonov, P. H. Beton, S. V. Novikov, C. Jagadish, H. H. Tan, M. J. Ford, M. Toth, C. Bradac and I. Aharonovich, Nature Materials, 2020, DOI: 10.1038/s41563-020-00850-y.
12. J. Comtet, B. Grosjean, E. Glushkov, A. Avsar, K. Watanabe, T. Taniguchi, R. Vuilleumier, M.-L. Bocquet and A. Radenovic, Nature Nanotechnology, 2020, 15, 598-604.
13. X. Xu, Z. O. Martin, D. Sychev, A. S. Lagutchev, Y. P. Chen, T. Taniguchi, K. Watanabe, V. M. Shalaev and A. Boltasseva, Nano Letters, 2021, 21, 8182-8189.
14. C. Li, N. Mendelson, R. Ritika, Y. Chen, Z.-Q. Xu, M. Toth and I. Aharonovich, Nano Letters, 2021, 21, 3626-3632.
15. R. N. E. Malein, P. Khatri, A. J. Ramsay and I. J. Luxmoore, ACS Photonics, 2021, 8, 1007-1012.
16. N. Chejanovsky, A. Mukherjee, J. Geng, Y.-C. Chen, Y. Kim, A. Denisenko, A. Finkler, T. Taniguchi, K. Watanabe, D. B. R. Dasari, P. Auburger, A. Gali, J. H. Smet and J. Wrachtrup, Nature Materials, 2021, 20, 1079-1084.
17. A. Gottscholl, M. Kianinia, V. Soltamov, S. Orlinskii, G. Mamin, C. Bradac, C. Kasper, K. Krambrock, A. Sperlich, M. Toth, I. Aharonovich and V. Dyakonov, Nature Materials, 2020, 19, 540-545.
18. H. L. Stern, Q. Gu, J. Jarman, S. Eizagirre Barker, N. Mendelson, D. Chugh, S. Schott, H. H. Tan, H. Sirringhaus, I. Aharonovich and M. Atatüre, Nature Communications, 2022, 13, 618.
19. W. Liu, Z.-P. Li, Y.-Z. Yang, S. Yu, Y. Meng, Z.-A. Wang, Z.-C. Li, N.-J. Guo, F.-F. Yan, Q. Li, J.-F. Wang, J.-S. Xu, Y.-T. Wang, J.-S. Tang, C.-F. Li and G.-C. Guo, ACS Photonics, 2021, 8, 1889-1895.
20. W. Liu, Z.-P. Li, Y.-Z. Yang, S. Yu, Y. Meng, Z.-A. Wang, N.-J. Guo, F.-F. Yan, Q. Li and J.-F. Wang, arXiv preprint arXiv:2101.11220, 2021.
21. A. Gottscholl, M. Diez, V. Soltamov, C. Kasper, A. Sperlich, M. Kianinia, C. Bradac, I. Aharonovich and V. Dyakonov, Science Advances, 2021, 7, eabf3630.
22. A. Gottscholl, M. Diez, V. Soltamov, C. Kasper, D. Krauße, A. Sperlich, M. Kianinia, C. Bradac, I. Aharonovich and V. Dyakonov, Nature Communications, 2021, 12, 4480.
23. X. Gao, S. Pandey, M. Kianinia, J. Ahn, P. Ju, I. Aharonovich, N. Shivaram and T. Li, ACS Photonics, 2021, 8, 994-1000.
24. X. Gao, B. Jiang, A. E. Llacsahuanga Allcca, K. Shen, M. A. Sadi, A. B. Solanki, P. Ju, Z. Xu, P. Upadhyaya, Y. P. Chen, S. A. Bhave and T. Li, Nano Letters, 2021, 21, 7708-7714.
25. M. Kianinia, S. White, J. E. Fröch, C. Bradac and I. Aharonovich, ACS Photonics, 2020, 7, 2147-2152.
26. J. R. Reimers, J. Shen, M. Kianinia, C. Bradac, I. Aharonovich, M. J. Ford and P. Piecuch, Physical Review B, 2020, 102, 144105.
27. P. Auburger and A. Gali, Physical Review B, 2021, 104, 075410.
28. V. Ivády, G. Barcza, G. Thiering, S. Li, H. Hamdi, J.-P. Chou, Ö. Legeza and A. Gali, npj Computational Materials, 2020, 6, 41.
29. F. F. Murzakhanov, B. V. Yavkin, G. V. Mamin, S. B. Orlinskii, I. E. Mumdzhi, I. N. Gracheva, B. F. Gabbasov, A. N. Smirnov, V. Y. Davydov and V. A. Soltamov, Nanomaterials, 2021, 11, 1373.
30. N. Mathur, A. Mukherjee, X. Gao, J. Luo, B. A. McCullian, T. Li, A. N. Vamivakas and G. D. Fuchs, arXiv preprint arXiv:2111.10855, 2021.
31. S. Baber, R. N. E. Malein, P. Khatri, P. S. Keatley, S. Guo, F. Withers, A. J. Ramsay and I. J. Luxmoore, Nano Letters, 2022, 22, 461-467.
32. J. E. Fröch, L. P. Spencer, M. Kianinia, D. D. Totonjian, M. Nguyen, A. Gottscholl, V. Dyakonov, M. Toth, S. Kim and I. Aharonovich, Nano Letters, 2021, 21, 6549-6555.
33. N. Mendelson, R. Ritika, M. Kianinia, J. Scott, S. Kim, J. E. Fröch, C. Gazzana, M. Westerhausen, L. Xiao, S. S. Mohajerani, S. Strauf, M. Toth, I. Aharonovich and Z.-Q. Xu, Advanced Materials, 2022, 34, 2106046.
34. E. Neu, P. Appel, M. Ganzhorn, J. Miguel-Sánchez, M. Lesik, V. Mille, V. Jacques, A. Tallaire, J. Achard and P. Maletinsky, Applied Physics Letters, 2014, 104, 153108.
35. M. Radulaski, M. Widmann, M. Niethammer, J. L. Zhang, S.-Y. Lee, T. Rendler, K. G. Lagoudakis, N. T. Son, E. Janzén, T. Ohshima, J. Wrachtrup and J. Vučković, Nano Letters, 2017, 17, 1782-1786.
36. J. Chaste, A. Missaoui, S. Huang, H. Henck, Z. Ben Aziza, L. Ferlazzo, C. Naylor, A. Balan, A. T. C. Johnson, R. Braive and A. Ouerghi, ACS Nano, 2018, 12, 3235-3242.
37. N.-J. Guo, W. Liu, Z.-P. Li, Y.-Z. Yang, S. Yu, Y. Meng, Z.-A. Wang, X.-D. Zeng, F.-F. Yan, Q. Li, J.-F. Wang, J.-S. Xu, Y.-T. Wang, J.-S. Tang, C.-F. Li and G.-C. Guo, ACS Omega, 2022, 7, 1733-1739.
38. A. O. Levchenko, V. V. Vasil'ev, S. A. Zibrov, A. S. Zibrov, A. V. Sivak and I. V. Fedotov, Applied Physics Letters, 2015, 106, 102402.
39. G.-Q. Liu, X. Feng, N. Wang, Q. Li and R.-B. Liu, Nature Communications, 2019, 10, 1344.
40. B. Liu, Q. Liao, X. Zhang, J. Du, Y. Ou, J. Xiao, Z. Kang, Z. Zhang and Y. Zhang, ACS Nano, 2019, 13, 9057-9066.
41. K. He, C. Poole, K. F. Mak and J. Shan, Nano Letters, 2013, 13, 2931-2936.

42. C. Palacios-Berraquero, D. M. Kara, A. R. P. Montblanch, M. Barbone, P. Latawiec, D. Yoon, A. K. Ott, M. Loncar, A. C. Ferrari and M. Atatüre, Nature Communications, 2017, 8, 15093.

43. A. Branny, S. Kumar, R. Proux and B. D. Gerardot, Nature Communications, 2017, 8, 15053.